

Optical observations of PSR J2021+3651 in the Dragonfly Nebula with the GTC¹

Aida Kirichenko^{1,2}, Andrey Danilenko¹, Peter Shternin^{1,2}, Yuriy Shibanov^{1,2},
 Elizaveta Ryspaeva², Dima Zyuzin¹, Martin Durant³, Oleg Kargaltsev⁴, George Pavlov⁵,
 and Antonio Cabrera-Lavers^{6,7}

ABSTRACT

PSR J2021+3651 is a 17 kyr old rotation powered pulsar detected in the radio, X-rays, and γ -rays. It powers a torus-like pulsar wind nebula with jets, dubbed the Dragonfly, which is very similar to that of the Vela pulsar. The Dragonfly is likely associated with the extended TeV source VER J2019+368 and extended radio emission. We conducted first deep optical observations with the GTC in the Sloan r' band to search for optical counterparts of the pulsar and its nebula. No counterparts were detected down to $r' \gtrsim 27.2$ and $\gtrsim 24.8$ for the point-like pulsar and the compact X-ray nebula, respectively. We also reanalyzed *Chandra* archival X-ray data taking into account an interstellar extinction – distance relation, constructed by us for the Dragonfly line of sight using the red-clump stars as standard candles. This allowed us to constrain the distance to the pulsar, $D = 1.8_{-1.4}^{+1.7}$ kpc at 90% confidence. It is much smaller than the dispersion measure distance of ~ 12 kpc but compatible with a γ -ray “pseudo-distance” of 1 kpc. Based on that and the optical upper limits, we conclude that PSR J2021+3651, similar to the Vela pulsar, is a very inefficient nonthermal emitter in the optical and X-rays, while its γ -ray efficiency is consistent with an average efficiency for γ -pulsars of similar age. Our optical flux upper limit for the pulsar is consistent with the long-wavelength extrapolation of its X-ray spectrum while the nebula flux upper limit does not constrain the respective extrapolation.

¹Ioffe Institute, Politekhnikeskaya 26, St. Petersburg, 194021, Russia

²St. Petersburg Polytechnic University, Politekhnikeskaya 29, St. Petersburg, 195251, Russia

³Department of Medical Biophysics, Sunnybrook Hospital M6 623, 2075 Bayview Avenue, Toronto M4N 3M5, Canada

⁴Department of Physics, The George Washington University, Washington, DC 20052, USA

⁵Department of Astronomy & Astrophysics, Pennsylvania State University, 525 Davey Lab, University Park, PA 16802, USA

⁶Instituto de Astrofísica de Canarias, E-38205 La Laguna, Tenerife, Spain

⁷Universidad de La Laguna, Dept. Astrofísica, E-38206 La Laguna, Tenerife, Spain

Subject headings: stars: neutron – pulsars: general – pulsars: individual: PSR J2021+3651

1. Introduction

The 104 ms pulsar J2021+3651 was discovered in the radio with the Arecibo telescope in a deep search for radio pulsations towards unidentified *ASCA* X-ray sources spatially coinciding with *EGRET* γ -ray objects (Roberts et al. 2002). With the characteristic age $\tau_c \approx 17$ kyr and spin-down luminosity $\dot{E} \approx 3.4 \times 10^{36}$ erg s $^{-1}$ this pulsar is among the youngest and most energetic rotation-powered pulsars known. The canonical dipole magnetic field estimated from the pulsar period and its derivative is $B \approx 3.2 \times 10^{12}$ G. A tentative detection of γ -ray pulsations with the pulsar period in the *EGRET* data was reported by McLaughlin & Cordes (2003). Later γ -ray observations with *AGILE* satellite (Halpern et al. 2008) and *Fermi* observatory (Abdo et al. 2009) firmly established a double-peaked pulse profile and a power-law spectrum with a photon index $\Gamma \sim 1.7$ and cutoff energy of ~ 2.9 GeV (Abdo et al. 2013). PSR J2021+3651 was also identified in X-rays with *Chandra*, and weak pulsations, also with the double-peaked profile, were detected at a 4σ significance (Hessels et al. 2004; Abdo et al. 2009). The pulsar X-ray spectrum contains thermal and non-thermal components from the surface and magnetosphere of a neutron star (NS), respectively (Van Etten et al. 2008). *Chandra* also revealed an extended pulsar wind nebula (PWN) G75.2+0.1 whose brightest internal part, within $\sim 30''$ of the pulsar, has a torus-like morphology with axial jets. By its specific spatial shape this PWN was dubbed the Dragonfly Nebula (Van Etten et al. 2008). A fainter diffuse emission is extended up to several arcminutes.

The PSR J2021+3651 position is projected on the Cygnus-X region, one of the richest known regions of star formation in the Galaxy. A bright extended TeV source MGRO J2019+37 was identified with the *Milagro* sky survey in this region with a 20 TeV flux of 80% of those of the Crab Nebula (Abdo et al. 2007). The source was suggested to be associated with the Dragonfly, which was recently confirmed by observations with the VERITAS observatory. VERITAS resolved the source into two objects (Aliu et al. 2014). The brightest one, VER J2019+368, has a hard spectrum resembling the spectrum of Vela X – a TeV PWN system powered by the Vela pulsar. VER J2019+368 coincides also with an extended region of non-thermal radio emission.

The most controversial parameter of PSR J2021+3651 is the distance. The NE2001 model for the Galactic distribution of free electrons (Cordes & Lazio 2002) for the pulsar line of sight ($l = 75^\circ 21'$, $b = 0^\circ 11'$) and the dispersion measure $DM \approx 370$ pc cm $^{-3}$ yield a distance $D \approx 12$ kpc (e.g., Roberts et al. 2002). Comparing a hydrogen absorbing column density obtained from first X-ray observations and the total Galactic HI column density along the pulsar line of sight, Hessels et al.

¹Based on observations made with the Gran Telescopio Canarias (GTC), installed in the Spanish Observatorio del Roque de los Muchachos of the Instituto de Astrofísica de Canarias, in the island of La Palma, programme GTC3-11B.

(2004) suggested $D \approx 10$ kpc. Van Etten et al. (2008) performed similar analysis of subsequent deeper X-ray observations and found the distance of 3–4 kpc. The pulsar polarization rotation measure implies a minimal $D \approx 5$ kpc (Abdo et al. 2009). Adopting the latter value and assuming that PSR J2021+3651 was born near the center of VER J2019+368, Aliu et al. (2014) estimated a possible transverse velocity of the pulsar to be ~ 840 km s $^{-1}$, which is about 3 times higher than the average for pulsar velocities (Hobbs et al. 2005). Finally, the distance can be as low as 1.5 kpc if the pulsar is located within the Cygnus-X region. This location is consistent with the empirical γ -ray “pseudo-distance” relation (e.g., Saz Parkinson et al. 2010) suggesting $D \sim 1$ kpc.

By many multiwavelength properties PSR J2021+3651 and its PWN are similar to the Vela pulsar plus PWN system, but, in contrast to the Vela, this pulsar has never been studied in the optical. We report first deep optical observations of the PSR J2021+3651 field performed with the 10.4-m Gran Telescopio Canarias (GTC). We also address the issue of the distance discrepancies, using the *Chandra* archival X-ray data and red-clump stars as standard candles, and compare the optical results with the X-ray ones. The details of observations and data reduction are described in Sect. 2, our results are presented in Sect. 3 and are discussed in Sect. 4.

2. GTC data

2.1. Observations and data reduction

The pulsar field was imaged with the Optical System for Imaging and low-intermediate Resolution Integrated Spectroscopy (OSIRIS²) in the Sloan r' band at the GTC on 2011 September 28. Sixteen dithered 158-second exposures were obtained using the OSIRIS standard image scale of $0''.254/\text{pixel}$ with the field of view of $7'.8 \times 7'.8$. The field was exposed on a mosaic of two CCDs, with the target source placed on CCD2. The observations were carried out during dark time, and the conditions were photometric, with seeing varying from $0''.8$ to $1''.1$.

Standard data reduction and analysis, including bias subtraction and flat-fielding, was performed with IRAF tools. To eliminate shifts between individual exposures, we collected a set of unsaturated stars in the field and aligned the images to the one with the best seeing using IRAF routines. The alignment uncertainty was $\lesssim 0.1$ pixel. All exposures were then combined and yielded a final image with a mean seeing of $0''.9$, airmass of 1.8, and total integration time of ≈ 2.5 ks.

²For instrument details see <http://www.gtc.iac.es/instruments/osiris/>

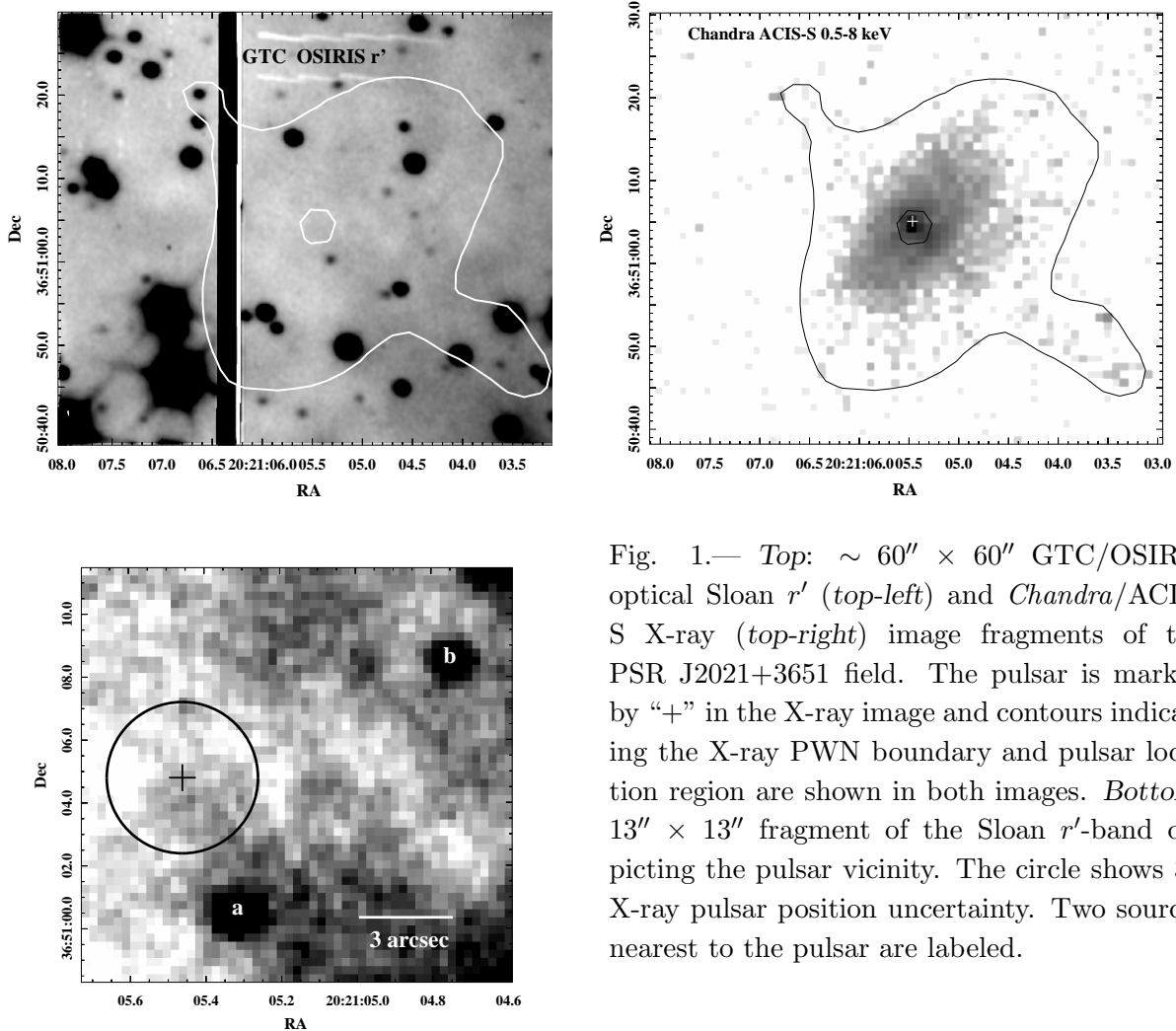


Fig. 1.— *Top*: $\sim 60'' \times 60''$ GTC/OSIRIS optical Sloan r' (*top-left*) and *Chandra*/ACIS-S X-ray (*top-right*) image fragments of the PSR J2021+3651 field. The pulsar is marked by “+” in the X-ray image and contours indicating the X-ray PWN boundary and pulsar location region are shown in both images. *Bottom*: $13'' \times 13''$ fragment of the Sloan r' -band depicting the pulsar vicinity. The circle shows 3σ X-ray pulsar position uncertainty. Two sources nearest to the pulsar are labeled.

2.2. Astrometric referencing and photometric calibration

For astrometric referencing, positions of 10 suitable astrometric standards from the USNO-B1.0 catalogue³ were used. Their pixel coordinates were measured on the combined image with the IRAF task *imcenter*. The IRAF *ccmap* routine was applied to the astrometric transformation of the image. Formal *rms* uncertainties of the astrometric fit for the combined image were $\Delta RA \lesssim 0''.17$ and $\Delta Dec \lesssim 0''.13$. Accounting for the nominal catalog uncertainty of $\approx 0''.2$, this results in conservative estimates of 1σ referencing uncertainties of $\lesssim 0''.26$ for RA and $\lesssim 0''.24$ for Dec.

The photometric calibration was carried out with G158-100 Sloan standard observed the same

³<http://www.nofs.navy.mil/data/fchpix/>

night as our target. The atmospheric extinction of 0.10 ± 0.01 mag airmass⁻¹ for the Sloan r' -band was taken from the OSIRIS user manual. The resulting magnitude zero-point for our r' image is $29^m13 \pm 0^m02$.

3. Results

3.1. Searching for the Dragonfly and pulsar optical counterparts

The $60'' \times 60''$ pulsar field fragment of the GTC/OSIRIS r' -band image, which contains the brightest part of the Dragonfly Nebula, is shown in the top-left panel of Figure 1. The image is smoothed with a Gaussian kernel with width $\sigma = 2$ pix. It is compared with the respective *Chandra*/ACIS-S 0.5–8 keV X-ray image (top-right panel of Figure 1), obtained by merging all the available archival data⁴ (112 ks effective exposure in total). The data were reprocessed with the CIAO v.4.6 *chandra_repro* tool with CALDB v.4.5.9. The X-ray image is binned by two ACIS pixels, smoothed with one-pixel Gaussian kernel, and shown in log-intensity scale. The X-ray PWN is comprised of a SW jet, NE counter-jet, and two arcs, which are oriented perpendicular to the jets. The arcs are believed to be associated with the PWN equatorial torus seen almost edge on (Hessels et al. 2004; Van Etten et al. 2008). Contours in the X-ray image indicate the outer boundary of the torus-like PWN, where it blends with the background, and the region around the pulsar (marked by the cross). In the top left panel of Figure 1 the X-ray contours are overlaid on the optical image. The vertical bold strip crossing the left side of the optical image is a bleed line from a bright over-saturated background star located outside the fragment. Two wave-shaped horizontal curves near the top side of the image are detector artifacts. Comparing the optical and X-ray images, we do not find any significant extended optical feature correlated with the X-ray morphology of the compact Dragonfly PWN. However, at an arcminute scale comparable to the faint diffuse X-ray emission extent, there are some background variations containing bright and dark regions seen in all individual exposures as well. Examination of $H\alpha$ images of the field from the INT Photometric Survey of the Northern Sky (Barentsen et al. 2014) shows that these variations correlate with the $H\alpha$ emission variations.

The immediate pulsar vicinity is enlarged in the left-bottom panel of Figure 1, where the $r \approx 2''.4$ circle is centered at the pulsar X-ray position with RA = 20:21:05.46 and Dec = +36:51:04.8 (Hessels et al. 2004). It corresponds to the 3σ pulsar position uncertainty which accounts for the optical astrometric referencing and pulsar X-ray position uncertainties. No significant point-like objects are detected within the pulsar error circle. The closest reliably detected point-like source “a” with $r' = 24.40 \pm 0.04$ is located at about $4''.8$ or at $\approx 6\sigma$ from the pulsar X-ray position. More distant object “b” has a lower brightness of $25^m01 \pm 0^m05$ and is located at $\approx 9''.4$ or about 12σ

⁴PI Roberts, *Chandra*/ACIS-S, OBsID 3901, date of obs. 2003-02-12, 19 ks exposure; PI Romani, *Chandra*/ACIS-S, OBsIDs 7603 and 8502, date of obs. 2006-12-29 59+34 ks exposure

from the pulsar. Because of their large offsets, both sources are unrelated to the pulsar.

Using our optical image we, therefore, can set only upper limits on the pulsar and the Dragonfly Nebula flux densities in the Sloan r' band. For the pulsar, we used a mean background deviation within a circular aperture with a 4 pixel ($\approx 1''$) radius centered at the pulsar position. We accounted for an aperture correction of 0^m1 derived using bright background stars. The resulting 3σ upper limit on the pulsar flux density is $\lesssim 0.04 \mu\text{Jy}$ ($r' \gtrsim 27.2$). For the nebula, we used an elliptical aperture with semi-axes of $6''.2$ and $10''.6$ and a position angle of 137° centered at the pulsar, which encapsulates most of the X-ray PWN equatorial torus emission. The 3σ upper limit on the spatially integrated flux density of the PWN is $\lesssim 0.36 \mu\text{Jy}$ ($r' \gtrsim 24.8$).

3.2. Distance and interstellar extinction

It is possible to construct an extinction–distance relation for the direction towards the pulsar utilizing red-clump stars as standard candles, following a method described, for instance, in López-Corredoira et al. (2002) and Cabrera-Lavers et al. (2005). The method was used previously to constrain distances and extinctions for several sources. Some examples are the X-ray binary 4U 1608–52 (Güver et al. 2010), six anomalous X-ray pulsars (Durant & van Kerkwijk 2006), and two γ -ray pulsars (Danilenko et al. 2012, 2013).

In the top panel of Figure 2, we show K vs $J - K$ band color-magnitude diagram for stars from the 2MASS All-Sky Point Source Catalogue⁵ located within $0^\circ3$ of the pulsar position. The red-clump (RC) branch, as well as main-sequence (MS) and asymptotic-giant (AGB) branches, are indicated. We divided the diagram into several magnitude bins, and in each bin we fitted $J - K$ color distribution with a mixture of two Gaussians corresponding to the MS and RC branches. The AGB stars were eliminated by omitting all points located right of a boundary starting at $J - K = 1.7$ for small magnitudes and ending at 2^m5 for large ones. The derived $J - K$ colors of RC stars with their uncertainties were then transformed into distances and interstellar extinctions A_V , using relations from Rieke & Lebofsky (1985), assuming the absolute magnitude and the intrinsic color of the red-clump stars to be $M_K = -1.62 \pm 0.03$, and $(J - K)_0 = 0.68 \pm 0.07$, respectively (see the above-cited papers for details). Extinctions were transformed to hydrogen absorbing column densities N_{H} using a standard empirical relation $N_{\text{H}} = A_V \times (1.79 \pm 0.03) \times 10^{21} \text{ cm}^{-2}$ (Predehl & Schmitt 1995).

The resulting N_{H} –distance dependence is shown in the bottom panel of Figure 2. N_{H} increases with the distance reaching a limit of $(15 \pm 4) \times 10^{21} \text{ cm}^{-2}$ at distances $\gtrsim 5$ kpc. Within uncertainties this limit is consistent with the total Galactic N_{H} in the pulsar direction of $\approx 12 \times 10^{21}$ and $\approx 9.7 \times 10^{21} \text{ cm}^{-2}$, estimated from the HI maps provided by Dickey & Lockman (1990) and Kalberla et al. (2005), respectively. Corresponding $A_V = 8.4 \pm 2.2$ is also compatible with the entire Galactic extinction estimate of $\sim 11^m0$ (Schlafly & Finkbeiner 2011), although the respective extinction map

⁵see <http://irsa.ipac.caltech.edu/applications/DataTag/>, DataTag = ADS/IRSA.Gator#2014/0814/100517_7624

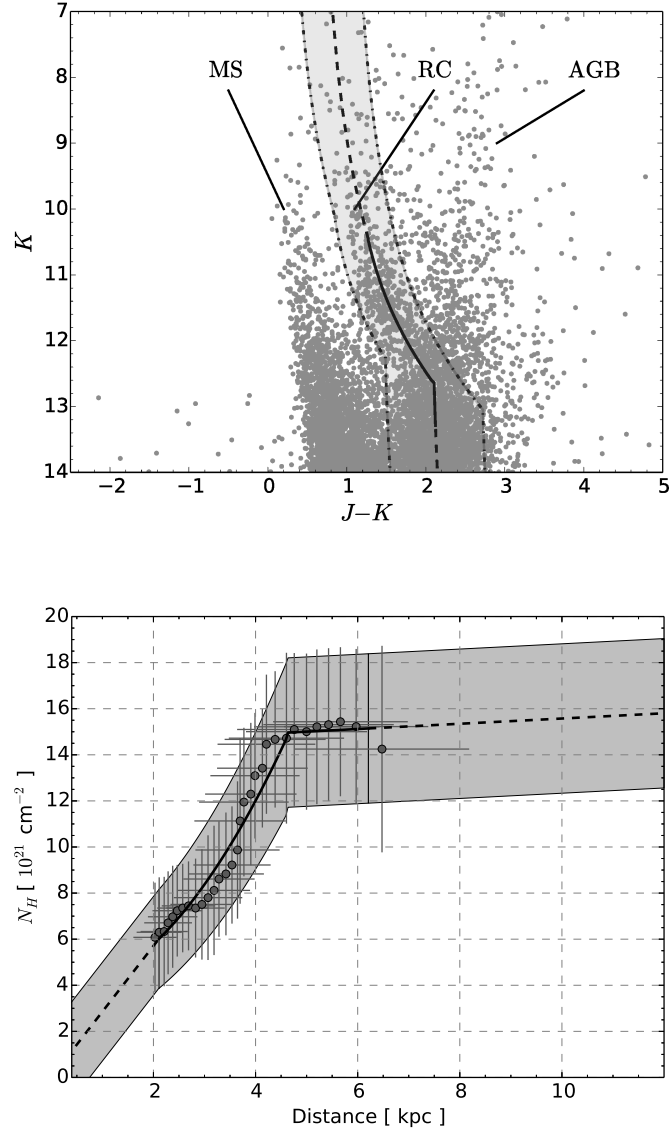


Fig. 2.— *Top*: K vs $J-K$ diagram for the stars from the 2MASS All-Sky Point Source Catalogue located within $0^\circ.3$ of the pulsar position ($l = 75^\circ.22$, $b = 0^\circ.11$). The main-sequence (MS), red-clump (RC), and asymptotic-giant (AGB) branches are indicated. Solid line shows a smoothed spline approximation to the RC stars mean colors; dashed segments are its extrapolations to higher and lower K magnitudes. Light-shaded region bounded by dot-dashed lines contains 95% (2σ) of RC stars. *Bottom*: Empirical N_H –distance relation for the PSR J2021+3651 direction derived using the RC stars colors from the diagram at the *top* panel. Bars are 1σ uncertainties. The solid line and gray filled region are smoothing spline approximations to the data points and their uncertainties, respectively. They are linearly extrapolated to small and large distances (dashed lines).

is considered as not reliable at $b \lesssim 5^\circ$.

3.3. X-ray spectral analysis

We reanalyzed the archival *Chandra* data in light of the N_{H} –distance relation. We extracted the pulsar spectra from all three *Chandra*/ACIS-S sets using an aperture with a radius of $0''.74$ centered at the pulsar position applying the CIAO v.4.6 *specextract* tool. We also extracted the PWN spectrum from an elliptical region with semi-axes of $6''.2$ and $10''.6$ and a position angle of 137° , that encloses most of the PWN equatorial torus emission. The circle aperture of a $2''$ radius around the pulsar was excluded from this region. Backgrounds were taken from regions free of any sources on the ACIS-S3 chip, where the Dragonfly was exposed in all three *Chandra* data sets with live times of 19, 59, and 43 ks. Total numbers of source counts are ≈ 1270 for the pulsar and ≈ 5250 for the PWN.

To evaluate likelihoods, we used the χ^2 statistics. To model the pulsar spectrum, we applied an absorbed sum of the power-law (PL) and thermal components. Any single component did not describe the data. For the thermal component, we tried blackbody (BB) and magnetic neutron star hydrogen atmosphere models NSA (Pavlov et al. 1995) and NSMAX (Ho et al. 2008). For the interstellar absorption, we used the XSPEC photoelectric absorption *phabs* model with default cross-sections *bcmc* (Balucinska-Church & McCammon 1992) and abundances *angr* (Anders & Grevesse 1989).

To model the contribution of the PWN to the spectrum extracted from the pulsar aperture, we added second PL to the pulsar spectral model and fitted the PSR and PWN spectra simultaneously in the 0.3–10 keV spectral range. The second PL component photon index was tied with the PWN photon index, and N_{H} was set as a global parameter. Doing this, we also took into account the ratio of the PWN flux within the pulsar aperture to the total PWN flux of ≈ 0.05 , as it was estimated by Van Etten et al. (2008) and independently confirmed by us via modeling of *Chandra*/ACIS PSF.

The N_{H} –distance relation and its uncertainty were approximated by smoothing splines, shown by the line and gray filled region in the bottom panel of Figure 2. This relation was then used as a Bayesian prior information for the subsequent spectral fitting procedure (see, e.g., Gelman et al. 2003, for details). Technically, we assumed that for each distance the N_{H} value follows a Gaussian distribution with the mean and σ taken from the approximations. We then run Markov chain Monte Carlo (MCMC) using the Goodman-Weare algorithm implemented as a python package *emcee* by Foreman-Mackey et al. (2013). For each model we kept 1000 steps after initial burn-in, which is large enough considering that typical autocorrelation time (see, e.g. Goodman & Weare 2010) was of order of several tens (50–90) of iterations. As 100 MCMC walkers (Goodman & Weare 2010) was used, we obtained 100000 samples in total.

Posterior median values of spectral parameters with 90% credible intervals for the BB+PL and NSMAX+PL models are presented in Table 1. The goodness-of-fit test (χ^2 values are in Table 1)

shows that both models are equally consistent with the data. We present fit results for only one of hydrogen atmosphere models, NSMAX 1260, which corresponds to the surface magnetic field $B = 4 \times 10^{12}$ G (Ho et al. 2008). The thermal component can be equally well fitted by NSA or by any other model from the NSMAX set; the resulting parameters do not depend appreciably on the choice of specific atmosphere model. We prefer more modern NSMAX models because they account for the partial ionization in stellar atmospheres, especially important at low temperatures (as in our case), while the NSA models were constructed for fully ionized NS atmospheres.

Our results are generally consistent with those presented by Hessels et al. (2004) and Van Etten et al. (2008). However, in contrast to Van Etten et al. (2008), we did not fix N_{H} at a best-fit value obtained from a separate analysis of the PWN spectrum. Nevertheless, the resulting N_{H} is defined mainly by the PWN spectrum, and consistent with the one obtained by Van Etten et al. (2008) within uncertainties. Thereby it weakly depends on a particular model used to describe the pulsar spectrum and on a particular $N_{\text{H}}-D$ relation. The distance $D = 1.8_{-1.4}^{+1.7}$ kpc⁶ is now mainly determined by N_{H} and the adopted $N_{\text{H}}-D$ relation. In this approach, only two parameters are defined by the thermal component: the radius R and the effective temperature T of the emitting area. Importantly, we were able to infer the absolute value of the radius R , not only the R/D ratio as it would have been without accounting for the $N_{\text{H}} - D$ relation. As it is typical for pulsars where X-ray spectral data can be equally well fitted by the blackbody and NS atmosphere models (e.g., Pavlov et al. 2001; Kirichenko et al. 2014), for the BB model R is a factor of 10 smaller and T is a factor of 2.5 larger than those for the hydrogen atmosphere model. For the latter, $R = 12_{-10}^{+20}$ km implies that emission can come from the bulk of the NS surface with the effective surface temperature, redshifted for distant observer, $T = 63_{-8}^{+9}$ eV, close to that of the Vela pulsar (Pavlov et al. 2001). For the BB model, $R = 1.3_{-1.0}^{+1.5}$ km, which is compatible with a canonical pulsar hot polar cap radius of ~ 0.6 km for a 100-ms pulsar (Sturrock 1971).

⁶Here and below we discuss the largest D range from Table 1.

Table 1: Posterior medians for the pulsar and the PWN equatorial torus region spectra. The BB+PL and NSMAX+PL models are for the pulsar spectrum, while the PWN is described by the PL model †.

Model	N_{H} 10^{21} cm^{-2}	Γ_{psr}	$K^{\text{psr}} \ddagger$ 10^{-5} photons $\text{keV}^{-1} \text{ cm}^{-2} \text{ s}^{-1}$	T eV	R km	D kpc	Γ_{pwn}	$K^{\text{pwn}} \ddagger$ 10^{-5} photons $\text{keV}^{-1} \text{ cm}^{-2} \text{ s}^{-1}$	χ^2 (dof)
BB+PL	$5.8_{-0.5}^{+0.5}$	$1.8_{-0.6}^{+0.6}$	$1.0_{-0.6}^{+1.0}$	155_{-14}^{+14}	$1.3_{-1.0}^{+1.5}$	$1.8_{-1.4}^{+1.5}$	$1.4_{-0.1}^{+0.1}$	$9.7_{-0.9}^{+1.0}$	459(469)
NSMAX+PL	$6.0_{-0.5}^{+0.5}$	$1.3_{-0.8}^{+0.7}$	$0.5_{-0.4}^{+0.7}$	63_{-8}^{+9}	$12.0_{-9.6}^{+19.5}$	$1.8_{-1.4}^{+1.7}$	$1.4_{-0.1}^{+0.1}$	$10.0_{-0.9}^{+1.0}$	472(469)

† N_{H} is the absorbing column density. The temperatures T and emitting area radii R for the BB and NSMAX spectral components are given as measured by a distant observer. For the NSMAX component, the gravitation redshift $1+z = (1 - 2.952M/R)^{-0.5}$, where M and R are the NS mass and circumferential radius in the Solar mass and km units, respectively, is fixed at 1.21. This corresponds to a canonical NS with $M = 1.4$ and $R = 13$ km. $K^{\text{psr,pwn}}$ and $\Gamma_{\text{psr,pwn}}$ are PL normalizations and photon spectral indexes for the pulsar (psr) and PWN (pwn), respectively. All errors correspond to 90% credible intervals derived via MCMC.

‡ Pulsar fluxes in 2–10 keV range are $\log F_{\text{X}}^{\text{psr}} = -13.5_{-0.8}^{+0.7}, -13.4_{-1.2}^{+1.0}$ [$\text{erg cm}^{-2} \text{ s}^{-1}$], for BB+PL and NSMAX+PL models, respectively. PWN flux in the same range is $\log F_{\text{X}}^{\text{pwn}} = -12.2_{-0.1}^{+0.1}$ [$\text{erg cm}^{-2} \text{ s}^{-1}$] for both models.

3.4. Multiwavelength spectra of the pulsar and PWN

The best-fit N_{H} values obtained from the X-ray spectral analysis suggest a total interstellar extinction towards the Dragonfly $A_V \approx 3.3$ in the V band, which results in the extinction $A_{r'} \approx 2.8$ in the r' band using a standard extinction law with $R_V = 3.1$ (Cardelli et al. 1989). Based on this, upper limits on the dereddened flux densities for the pulsar and PWN in the r' band are about $0.57 \mu\text{Jy}$ and $4.85 \mu\text{Jy}$, respectively. In Figure 3 we compare these limits with unabsorbed X-ray spectra of the pulsar (top panel) and PWN (bottom panel), fitted by BB+PL and PL models, respectively. For the PWN, the optical and X-ray data were obtained from the same spatial region enclosing its X-ray equatorial torus emission (see Sect. 3.1, 3.3, and Figure 1). The solid line in the top panel of Figure 3 shows the total best-fit model, including the contribution of PWN nonthermal photons to the spectrum extracted from the pulsar aperture. The dashed line shows solely the PL component of the pulsar. As seen, the PWN contribution is substantial only in the high-energy tail.

As seen from Figure 3, the pulsar optical flux upper limit does not exceed the extrapolation of the best-fit X-ray spectral model to the optical. This is typical for rotation powered pulsars detected in the optical and X-rays (Danilenko et al. 2011; Durant et al. 2011; Mignani et al. 2010; Shibano et al. 2006). For all of them, the nonthermal component dominates in the optical. However, this component usually shows a break between the optical and X-rays with a significant spectral flattening in the optical. Our data do not exclude the presence of such a break for PSR J2021+3651, although the extrapolation of the X-ray PL component is still rather uncertain and the optical limit is not deep enough. The NSMAX+PL model, which equally well fits the X-ray data, does not change these conclusions.

All torus-like PWNe, which have been detected in both spectral domains, also show spectral flattening in the optical in comparison with X-rays (e.g., Zharikov et al. 2013). However, for the Dragonfly the situation is currently even less certain than for its pulsar. The nebula optical flux upper limit overshoots the low-energy extrapolation of its X-ray spectrum (bottom panel of Figure 3), and the presence of the break in the spectrum of this PWN remains an open question.

The dereddened upper limits were obtained using the $A_V - N_{\text{H}}$ relation of Predehl & Schmitt (1995). There exist other empirical relations of that kind. For instance, Güver & Özel (2009) give $N_{\text{H}} = A_V \times (2.21 \pm 0.09) \times 10^{21} \text{ cm}^{-2}$, also consistent with the results of Gorenstein (1975). Using this relation instead, we get smaller $A_V \approx 2.7$ and hence dereddened upper limits a smaller by a factor of 1.6, which does not change general conclusions of this Section.

4. Discussion

Our rather deep, down to $r' \approx 27.2$, GTC optical imaging of the Dragonfly Nebula field allowed us to set upper limits on the optical flux densities of PSR J2021+3651 and its PWN. The non-detection of this energetic system can be attributed to high interstellar extinction towards

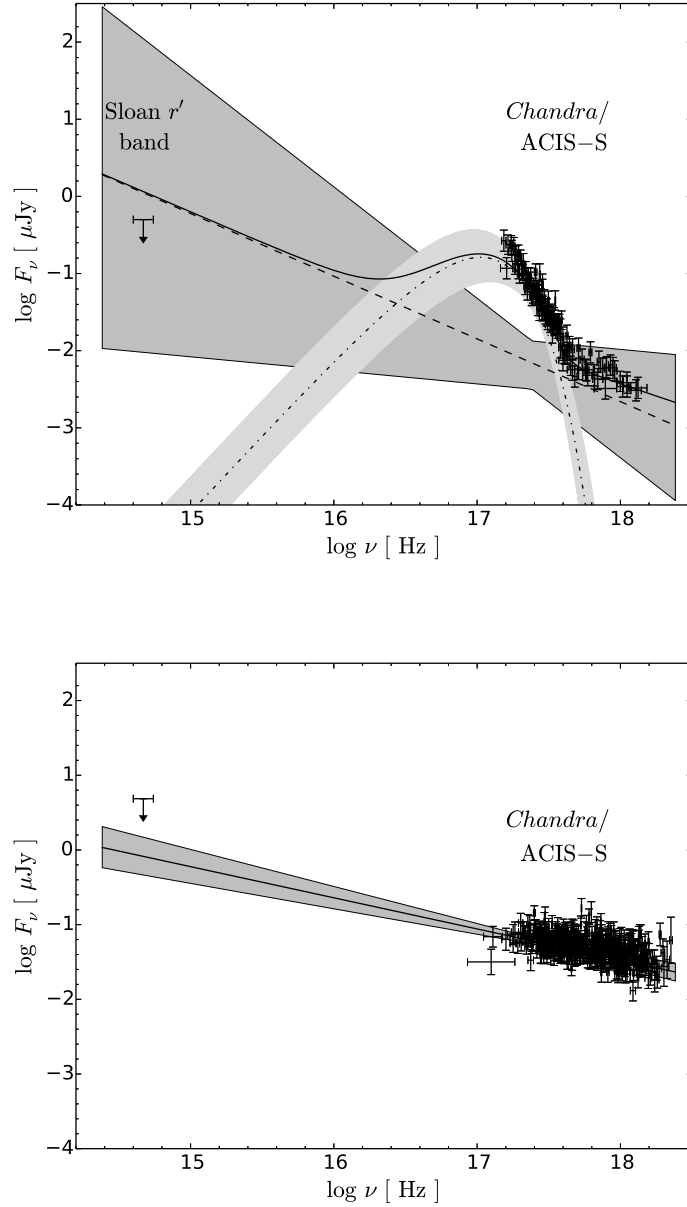


Fig. 3.— *Top*: Unabsorbed spectrum of PSR J2021+3651. The solid line is the best-fit model for the *Chandra* X-ray spectrum which includes BB and PL pulsar spectral components and the PWN contribution to the spectral extraction aperture (see text for details). The best-fit model is extrapolated towards the optical. The GTC dereddened 3σ flux upper limit in the r' band is shown by the bar with the arrow. Dash-dotted and dashed lines with light- and dark-gray regions are the BB and PL pulsar spectral components with their 90% uncertainties, respectively. The difference between the solid and dashed lines is clearly visible at the high-energy tail and reflects the PWN contribution. *Bottom*: The solid line and gray region are the best-fit PL model of the X-ray spectrum of the PWN equatorial torus region with its 90% uncertainties, respectively. The GTC dereddened optical 3σ flux upper limit for this region in the r' band is also shown. The error-bar crosses in each panel are the unfolded *Chandra* data.

the object, which is roughly about of 3^m in the r' band. Considering the data for other pulsars detected in the optical and X-rays, we conclude that 1–2 magnitude deeper optical observations are necessary to detect this pulsar and to reveal the expected spectral break between the optical and X-rays. This is, in principle, feasible with 8–10 m ground-based telescopes, such as the GTC, using a few hour exposure in r' at good seeing conditions, although observations at longer wavelengths, less affected by the interstellar absorption, would be preferable. Such observations would also be useful to better constrain the optical-X-ray spectral properties of the PWN.

Our N_{H} –distance relation, constructed using the red-clump star method and compiled with the X-ray spectral analysis, supports previous suggestions that the pulsar is likely to be substantially closer to us than it is inferred from DM and the NE2001 model of the Galactic distribution of free electrons. Our estimate $D = 1.8_{-1.4}^{+1.7}$ kpc is compatible, within uncertainties, with the 3–4 kpc range suggested by Van Etten et al. (2008). However, our allowed distance range is shifted to lower distances. It suggests the association of the pulsar with the Cygnus-X region, located within 2 kpc from the Sun, and is consistent with the γ -ray “pseudo-distance” of ~ 1 kpc provided by the *Fermi* data. The reduced distance we found makes feasible parallax and pulsar proper motion measurements with VLBI. A possible source of systematic errors in our distance determination method originates from ambiguity in $A_V - N_{\text{H}}$ relations, as stated above. Reprocessing the analysis of Sections 3.2 and 3.3 using the relation of Güver & Özel (2009), we obtain an even smaller distance of $1.3_{-1.1}^{+1.5}$ kpc.

Comparing the DM of 370 pc cm^{-3} , or electron column density $N_e \approx 1.14 \times 10^{21} \text{ cm}^{-2}$, with N_{H} of $6 \times 10^{21} \text{ cm}^{-2}$ leads to an average ionization ratio of 19% along the pulsar line of sight which is not too much larger than the 10% ionization found on average (e.g., He et al. 2013, figure 1). On the other hand, the NE2001 electron density model in the pulsar direction gives much smaller $N_e = 0.7_{-0.6}^{+1.2} \times 10^{20} \text{ cm}^{-2}$ for distance range of $D = 1.8_{-1.4}^{+1.7}$ kpc. There exist several indications that the NE2001 model strongly underestimates N_e in the vicinity of the PSR J2021+3651 direction (Camilo et al. 2009, 2012; Arumugasamy et al. 2014). For instance, there is another pulsar J2022+3842 at only 1°8 from PSR J2021+3651 with very high DM = 429 pc cm^{-2} , for which NE2001 model gives obviously overestimated distance $D > 50$ kpc (Arumugasamy et al. 2014). This may imply that there are dense clouds in the Cygnus-X region, which are not taken into account in the NE2001 model (Roberts et al. 2002).

As for the X-ray thermal emission component of PSR J2021+3651, we cannot state definitely whether the thermal emission comes from a hot polar cap or the bulk of the NS surface. This depends on which, BB or a hydrogen atmosphere, model is applied to describe the thermal emission. The phase-resolved spectroscopy would be useful to distinguish between the two possibilities. We note, however, that if the thermal emission originates from the entire surface of the star (the case of the atmospheric model), PSR J2021+3651 has a rather small surface temperature for its age. According to the NS cooling theories, such a small temperature can not be explained by a standard cooling scenario, but it can be reached if the effects of superfluidity in the stellar interiors are invoked. This is possible, for instance, if the powerful direct Urca process of neutrino emission

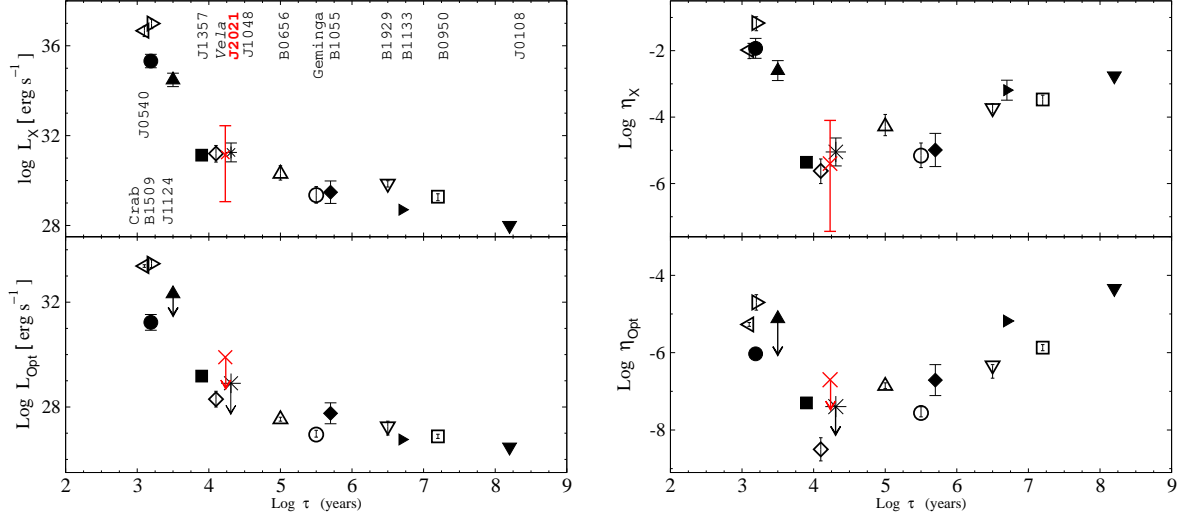


Fig. 4.— X-ray and optical luminosities, L_X and L_{Opt} , and respective efficiencies, η_X and η_{Opt} , for pulsars of different characteristic age τ detected in both spectral domains. The data are adopted from Danilenko et al. (2013). Different pulsars are marked by different symbols. The PSR J2021+3651 data, derived in this work, are included (marked by asterisk).

operates in the star but is suppressed by superfluidity (Yakovlev & Pethick 2004). In another interpretation the direct Urca process is not allowed, but the cooling is enhanced due to the specific process of the neutrino emission accompanying the Cooper pair formation in the neutron triplet superfluid. This is the essence of the so-called minimal cooling scenario (Gusakov et al. 2004; Page et al. 2004, 2009).

The pulsar’s 0.1–100 GeV γ -ray luminosity $L_\gamma \approx 5.9 \times 10^{36}$ erg s $^{-1}$ and efficiency $\eta_\gamma = L_\gamma / \dot{E} \approx 1.8$, derived in the 2nd Fermi Pulsar Catalog (Abdo et al. 2013) using the distance of 10 kpc from Hessels et al. (2004) appear to be unreasonably high, and place the pulsar at the highest end of L_γ and η_γ distributions of γ -ray pulsars. In contrast, for the distance $D = 1.8^{+1.7}_{-1.4}$ kpc inferred from our analysis, $\log L_\gamma = 35.3^{+0.6}_{-1.3}$ [erg s $^{-1}$] and $\log \eta_\gamma = -1.2^{+0.6}_{-1.3}$ become consistent with the average values of the respective distributions for γ -ray pulsars with similar \dot{E} and/or characteristic age (cf., Figures 9 and 10 of Abdo et al. 2013).

The pulsar’s unabsorbed nonthermal X-ray flux in 2–10 keV range, derived from the X-ray spectral fits, is $\log F_X = -13.5^{+0.7}_{-0.8}$ [erg cm $^{-2}$ s $^{-1}$]. The respective X-ray luminosity and efficiency are $\log L_X = 31.1^{+1.3}_{-2.1}$ [erg s $^{-1}$] and $\log \eta_X = -5.4^{+1.3}_{-2.0}$, assuming the distance range derived in this work.

For the 90% distance upper limit $D = 3.5$ kpc, upper limits on the optical luminosity and effi-

ciency in the V band, assuming a flat spectrum, are $\log L_{\text{Opt}} \lesssim 29.9$ [erg s^{-1}] and $\log \eta_{\text{Opt}} \lesssim -6.7$, respectively. In Figure 4 we compare the obtained X-ray and optical efficiencies and luminosities with the data for other pulsars observed in both ranges (Danilenko et al. 2013). According to Figure 4, we can conclude that PSR J2021+3651, like the Vela pulsar, is inefficient in these ranges as compared to other substantially younger and older pulsars. We thus obtain a new member of the small sample of Vela-like pulsars forming a puzzling minimum in the optical and X-ray efficiency dependences on age at a characteristic age of ~ 10 kyr noticed previously by Zharikov et al. (2006). No such minimum is visible in the respective γ -ray dependence (Abdo et al. 2013). Together with strong glitches and high polarization in the radio (Hessels et al. 2004), a bright NS thermal emission component in X-rays, a double arc X-ray PWN with jets (Van Etten et al. 2008), γ -ray activity (Abdo et al. 2009), and association with a TeV source (Aliu et al. 2014), this makes the Dragonfly pulsar and PWN remarkably similar to the Vela pulsar and its PWN.

We thank Dima Barsukov and Serge Balashev for helpful discussion and the anonymous referee for useful comments. The work was supported by the Russian Science Foundation, grant 14-12-00316. The scientific results reported in this article are partially based on data obtained from the Chandra Data Archive, observations made by the Chandra X-ray Observatory. The research has also made use of the NASA/IPAC Infrared Science Archive, which is operated by the Jet Propulsion Laboratory, California Institute of Technology, under contract with the National Aeronautics and Space Administration.

Facilities: Gran Telescopio Canarias, *CXO*.

REFERENCES

- Abdo, A. A., Allen, B., Berley, D., et al. 2007, *ApJ*, 664, L91
- Abdo, A. A., Ackermann, M., Ajello, M., et al. 2009, *ApJ*, 700, 1059
- Abdo, A. A., Ajello, M., Allafort, A., et al. 2013, *ApJS*, 208, 17
- Aliu, E., Aune, T., Behera, B., et al. 2014, *ApJ*, 788, 78
- Anders, E., & Grevesse, N. 1989, *Geochim. Cosmochim. Acta*, 53, 197
- Arumugasamy, P., Pavlov, G. G., & Kargaltsev, O. 2014, *ApJ*, 790, 103
- Balucinska-Church, M., & McCammon, D. 1992, *ApJ*, 400, 699
- Barentsen, G., Farnhill, H. J., Drew, J. E., et al. 2014, *MNRAS*, 444, 3230
- Cabrera-Lavers, A., Garzón, F., & Hammersley, P. L. 2005, *A&A*, 433, 173
- Camilo, F., Ray, P. S., Ransom, S. M., et al. 2009, *ApJ*, 705, 1

- Camilo, F., Kerr, M., Ray, P. S., et al. 2012, *ApJ*, 746, 39
- Cardelli, J. A., Clayton, G. C., & Mathis, J. S. 1989, *ApJ*, 345, 245
- Cordes, J. M., & Lazio, T. J. W. 2002, *ArXiv Astrophysics e-prints*, astro-ph/0207156
- Danilenko, A., Kirichenko, A., Mennickent, R. E., et al. 2012, *A&A*, 540, A28
- Danilenko, A., Kirichenko, A., Sollerman, J., Shibarov, Y., & Zyuzin, D. 2013, *A&A*, 552, A127
- Danilenko, A. A., Zyuzin, D. A., Shibarov, Y. A., & Zharikov, S. V. 2011, *MNRAS*, 415, 867
- Dickey, J. M., & Lockman, F. J. 1990, *ARA&A*, 28, 215
- Durant, M., Kargaltsev, O., & Pavlov, G. G. 2011, *ApJ*, 743, 38
- Durant, M., & van Kerkwijk, M. H. 2006, *ApJ*, 650, 1070
- Foreman-Mackey, D., Hogg, D. W., Lang, D., & Goodman, J. 2013, *PASP*, 125, 306
- Gelman, A., Carlin, J. B., Stern, H. S., & Rubin, D. B. 2003, *Bayesian Data Analysis*, 2nd edn., ed. C. Chatfield, M. Tanner, & J. Zidek, *Texts in Statistical Science* (Boca Raton, London, New York, Washington, D.C.: Chapman & Hall/CRC)
- Goodman, J., & Weare, J. 2010, *Comm. App. Math. Comp. Sci.*, 5, 65
- Gorenstein, P. 1975, *ApJ*, 198, 95
- Gusakov, M. E., Kaminker, A. D., Yakovlev, D. G., & Gnedin, O. Y. 2004, *A&A*, 423, 1063
- Güver, T., & Özel, F. 2009, *MNRAS*, 400, 2050
- Güver, T., Özel, F., Cabrera-Lavers, A., & Wroblewski, P. 2010, *ApJ*, 712, 964
- Halpern, J. P., Camilo, F., Giuliani, A., et al. 2008, *ApJ*, 688, L33
- He, C., Ng, C.-Y., & Kaspi, V. M. 2013, *ApJ*, 768, 64
- Hessels, J. W. T., Roberts, M. S. E., Ransom, S. M., et al. 2004, *ApJ*, 612, 389
- Ho, W. C. G., Potekhin, A. Y., & Chabrier, G. 2008, *ApJS*, 178, 102
- Hobbs, G., Lorimer, D. R., Lyne, A. G., & Kramer, M. 2005, *MNRAS*, 360, 974
- Kalberla, P. M. W., Burton, W. B., Hartmann, D., et al. 2005, *A&A*, 440, 775
- Kirichenko, A., Danilenko, A., Shibarov, Y., et al. 2014, *A&A*, 564, A81
- López-Corredoira, M., Cabrera-Lavers, A., Garzón, F., & Hammersley, P. L. 2002, *A&A*, 394, 883

- McLaughlin, M. A., & Cordes, J. M. 2003, ArXiv Astrophysics e-prints, astro-ph/0310748
- Mignani, R. P., Pavlov, G. G., & Kargaltsev, O. 2010, ApJ, 720, 1635
- Page, D., Lattimer, J. M., Prakash, M., & Steiner, A. W. 2004, ApJS, 155, 623
- . 2009, ApJ, 707, 1131
- Pavlov, G. G., Shibano, Y. A., Zavlin, V. E., & Meyer, R. D. 1995, in *The Lives of the Neutron Stars*, ed. M. A. Alpar, U. Kiziloglu, & J. van Paradijs, 71
- Pavlov, G. G., Zavlin, V. E., Sanwal, D., Burwitz, V., & Garmire, G. P. 2001, ApJ, 552, L129
- Predehl, P., & Schmitt, J. H. M. M. 1995, A&A, 293, 889
- Rieke, G. H., & Lebofsky, M. J. 1985, ApJ, 288, 618
- Roberts, M. S. E., Hessels, J. W. T., Ransom, S. M., et al. 2002, ApJ, 577, L19
- Saz Parkinson, P. M., Dormody, M., Ziegler, M., et al. 2010, ApJ, 725, 571
- Schlaflly, E. F., & Finkbeiner, D. P. 2011, ApJ, 737, 103
- Shibano, Y. A., Zharikov, S. V., Komarova, V. N., et al. 2006, A&A, 448, 313
- Sturrock, P. A. 1971, ApJ, 164, 529
- Van Etten, A., Romani, R. W., & Ng, C.-Y. 2008, ApJ, 680, 1417
- Yakovlev, D. G., & Pethick, C. J. 2004, ARA&A, 42, 169
- Zharikov, S., Shibano, Y., & Komarova, V. 2006, *Advances in Space Research*, 37, 1979
- Zharikov, S. V., Zyuzin, D. A., Shibano, Y. A., & Mennickent, R. E. 2013, A&A, 554, A120